Power Balance in Aerodynamic Flows

Mark Drela*

Massachusetts Institute of Technology, Cambridge, Massachusetts 02139

A control volume analysis of the compressible viscous flow about an aircraft is performed, including integrated propulsors and flow-control systems. In contrast to most past analyses that have focused on forces and momentum flow, in particular thrust and drag, the present analysis focuses on mechanical power and kinetic energy flow. The result is a clear identification and quantification of all the power sources, power sinks, and their interactions, which are present in any aerodynamic flow. The formulation does not require any separate definitions of thrust and drag, and hence it is especially useful for analysis and optimization of aerodynamic configurations that have tightly integrated propulsion and boundary-layer control systems.

Nomenclature

b, c	=	wingspan and chord
$C_{\mathcal{D}}$	=	dissipation coefficient
C_f	=	skin friction coefficient
D_i	=	induced drag
D_p	=	profile drag
D_w	=	wave drag
$d\mathcal{S}$	=	surface element of control volume
$d\mathcal{V}$	=	volume element of control volume
$\dot{E}_a$	=	axial kinetic energy deposition rate
$\dot{E}_p$	=	pressure-work deposition rate
$\dot{E}_v$	=	transverse (vortex) kinetic energy deposition rate
$\dot{E}_w$	=	lateral wave-outflow energy deposition rate
F_n	=	streamwise force from lateral outflow velocity V_n
F_u	=	streamwise force from axial velocity u
F_v	=	streamwise force from transverse velocities v, w
F_x, F_z	=	total streamwise, normal aerodynamic forces
H	=	boundary-layer shape parameter, $=\delta^*/\theta$
H^*	=	kinetic energy shape parameter, $=\theta^*/\theta$
$\dot{h}$	=	climb rate, $=V_\infty \sin\gamma$
$\dot{m}$	=	mass flow
$\hat{n}$	=	unit normal vector, out of control volume
P_K	=	kinetic energy inflow rate
P_S	=	shaft power
P_V	=	volumetric power
p, p_t	=	static pressure, total pressure
Re_c	=	chord Reynolds number, $=V_\infty c/\nu$
Re_θ	=	mom. thickness Reynolds number, $=u_e\theta/\nu$
T	=	thrust
t	=	time
u, v, w	=	perturbation velocities
u, w	=	shear layer velocities (in shear layer section)
$\boldsymbol{V}$	=	fluid velocity, $=(V_\infty + u)\hat{x} + v\hat{y} + w\hat{z}$
V_n	=	side cylinder normal velocity, $=vn_y + wn_z$
V^2	=	fluid speed squared, $=\boldsymbol{V}\cdot\boldsymbol{V}$
W	=	aircraft weight
x, y, z	=	Cartesian axes
Γ	=	airfoil circulation
γ	=	climb angle
δ_K	=	wake kinetic energy excess thickness
$\dot{\mathcal{E}}$	=	mechanical energy outflow rate
θ, δ^*	=	momentum, displacement thicknesses
θ^*, δ^{**}	=	kinetic energy, density-flux thicknesses
ϱ, μ	=	fluid density, viscosity
$\underline{\bar{\tau}}$	=	viscous stress tensor
$\boldsymbol{\tau}$	=	surface viscous stress vector, $=\underline{\bar{\tau}}\cdot\hat{n}$
Φ	=	dissipation rate

Subscripts

∞	=	freestream quantity
B	=	quantity on body surface
O	=	quantity on outer boundary
e	=	shear layer edge quantity

Superscripts

SC	=	quantity on side cylinder
TP	=	quantity on Trefftz plane

I. Introduction

NUMEROUS previous workers have analyzed the flow about an aerodynamic body via a control volume approach to relate the body forces to the wake and the flow far field. The early work of Betz [1], Jones [2], and Oswatisch [3] focused on drag, whereas Maskell [4] considered both lift and drag for incompressible flow, and Kroo [5] reviewed various techniques for induced drag prediction and reduction. The recent efforts of VanDam [6], Giles and Cummings [7], and Kusunose [8] have treated the general compressible case, also with enthalpy addition from engines. More recently, Méheut and Bailly [9] have done an overview and comparison of most of the previous analyses and approaches for the drag component, and introduce their own refinement. Spalart [10] performs an even more detailed analysis for the incompressible case using inner and outer expansions of the far wake, and identifies a higher-order far-field term in the overall axial force which has been previously neglected.

The goals of the previous developments have been to allow accurate wind-tunnel drag measurements from wake surveys, with or without wind-tunnel wall interference, and also to allow accurate drag computation from computational fluid dynamics (CFD) results despite the presence of imperfect freestream boundary conditions and numerical errors. Additional benefits have been the clear identification of drag-producing sources in the flow and the relation of experiments and CFD results to other classical analyses such as lifting-line theory.

All the previous work has focused almost exclusively on momentum equation analysis, giving relations for the aerodynamic lift and drag forces. The implied propulsive power was then simply defined to be drag × velocity. Thermodynamic and state relations were also introduced, but only as a means to relate velocity and pressure to enthalpy and entropy in the downstream wake. In

*T. J. Kohler Professor of Fluid Dynamics, Department of Aeronautics and Astronautics. Fellow AIAA.

contrast, the present analysis will begin with the mechanical energy equation from the outset, giving relations between mechanical power and dissipation in the flowfield. The result is especially applicable for evaluation of complex aerodynamic configurations, particularly ones with tightly integrated propulsion and boundary-layer control systems.

It is worthwhile here to mention related work done for turbomachinery applications. Denton and Cumpsty [11] and also Denton [12] examined the dissipation and associated entropy and loss generation mechanisms on turbomachinery blading, wakes, and tip gaps. Greitzer et al. [13] also did an overview and further analyses of various flow situations. In the context of the present work, the previous turbomachinery work would be particularly relevant for estimating the losses of flow-control systems and associated ducts and impellers.

II. Control Volume Definition

Figure 1 shows the control volume (CV) surrounding the flow around an aerodynamic body. The CV boundary $\mathcal{S}$ is partitioned into an inner boundary $\mathcal{S}_B$ lying on the body surface and an outer boundary $\mathcal{S}_O$ lying in the flowfield. Together with Gauss's theorem, we therefore have

$$\iiint \nabla \cdot (\,) \, \mathrm{d}\mathcal{V} = \oiint (\,) \cdot \hat{n} \, \mathrm{d}\mathcal{S} = \oiint (\,) \cdot \hat{n} \, \mathrm{d}\mathcal{S}_B + \oiint (\,) \cdot \hat{n} \, \mathrm{d}\mathcal{S}_O \tag{1}$$

where ( ) is any field vector quantity. The outer-boundary $\mathcal{S}_O$ portions will be assumed to be oriented so that 1) the downstream Trefftz plane portion $\mathcal{S}_O^{\mathrm{TP}}$ is oriented perpendicular to V_∞, and 2) the side cylinder portion $\mathcal{S}_O^{\mathrm{SC}}$ is parallel to V_∞. These restrictions will considerably simplify most of the integral expressions to be derived.

The distance to the outer boundaries is completely arbitrary. However, it will be highly advantageous to place them so that 1) all vortical fluid leaves via $\mathcal{S}_O^{\mathrm{TP}}$, while any supersonic oblique waves which are present leave via $\mathcal{S}_O^{\mathrm{SC}}$, and 2) the distance to the side cylinder is at least several times the wingspan of the configuration. Unlike the first set of restrictions, these two are not hard requirements; however, they do have the great advantage of isolating different physical flow processes in separate terms in the equations.

III. Periodic-Unsteady Treatment

The present work will address steady or periodic-unsteady aerodynamic flows. The latter case must be addressed, because mechanical propulsors, impellers, or even flapping wings are treated as part of the flowfield. Their periodic unsteadiness produces nonzero nonlinear-term contributions to the time-averaged flow.

Consider the periodic-unsteady velocity components $\tilde{u}$, $\tilde{v}$, which can be expanded about their mean values $\bar{u}$, $\bar{v}$ in the form

Fig. 1 Two-dimensional cutaway view of 3-D CV surrounding an aerodynamic body. The inner boundary $\mathcal{S}_B$ lies on the body and may cover moving elements (top propulsor) or hide them inside (bottom propulsor). Vortex-wake velocities v, w on Trefftz plane are not shown.

$$\tilde{u}(x, y, z, t) = \bar{u}(x, y, z) + \sum_{k=1}^{\infty} u_k(x, y, z) \sin \frac{2\pi k t}{t_p} \tag{2}$$

$$\tilde{v}(x, y, z, t) = \bar{v}(x, y, z) + \sum_{k=1}^{\infty} v_k(x, y, z) \sin \frac{2\pi k t}{t_p} \tag{3}$$

where t_p is the period. Time averaging the velocities and their quadratic products then gives

$$u(x, y, z) \equiv \frac{1}{t_p} \int_0^{t_p} \tilde{u} \, \mathrm{d}t = \bar{u} \tag{4}$$

$$uv(x, y, z) \equiv \frac{1}{t_p} \int_0^{t_p} \tilde{u} \, \tilde{v} \, \mathrm{d}t = \bar{u} \, \bar{v} + \sum_{k=1}^{\infty} \frac{1}{2} u_k v_k \tag{5}$$

which mimics the Reynolds-averaging procedure for turbulent flows. Similar expressions can be obtained for cubic or higher products. Also, phase differences can be introduced by adding cosine-expansion sums, which will also result in additional coefficient-product sums.

In brief, product quantities such as uv imply the presence of unsteady-coefficient-product sums such as $\sum \frac{1}{2} u_k v_k$, etc., which will be omitted for brevity in the expressions. These omitted sums are expected to be important only for cases with large-scale unsteadiness, such as flapping wings. For such cases, the missing sums can then always be added to the various CV quantity spatial integrands to obtain the exact time-average form.

IV. Mass and Momentum Analysis

Although this work will focus primarily on a mechanical energy analysis, a brief mass and force analysis is necessary to simplify the later results.

A. Mass Relation

The time-averaged mass continuity equation for fluid flow is as follows:

$$\nabla \cdot (\rho V) = 0 \tag{6}$$

As described in the previous section, the unsteady-coefficient-product sum $\sum \frac{1}{2} \rho_k V_k$ is implicitly present inside the divergence, but has been omitted for clarity. Forming the volume integral $\iiint \{\mathrm{Eq.}\,(6)\} \, \mathrm{d}\mathcal{V}$ over the CV and invoking relation (1) then gives the following integral mass equation:

$$\dot{m}_B = \dot{m}_O \tag{7}$$

$$\dot{m}_B = -\oiint \rho V \cdot \hat{n} \, \mathrm{d}\mathcal{S}_B = \dot{m}_{\mathrm{fuel}} \simeq 0 \tag{8}$$

$$\dot{m}_O = \oiint \rho V \cdot \hat{n} \, \mathrm{d}\mathcal{S}_O = \dot{m}_{\mathrm{fuel}} \simeq 0 \tag{9}$$

These will be used only to manipulate and simplify other subsequent integral relations. As indicated, the fuel mass flow will be considered negligible.

B. Momentum and Force Relations

The time-averaged momentum equation in divergence form is as follows:

$$\nabla \cdot (\rho V V) = -\nabla p + \nabla \cdot \bar{\bar{\tau}} \tag{10}$$

Forming the volume integral $\iiint \{\mathrm{Eq.}\,(10)\} \, \mathrm{d}\mathcal{V}$ over the CV and invoking relation (1) then gives the integral momentum equation

$$F_B = F_O \tag{11}$$

where the following definitions have been made.

Net force on body, including propulsors

$$F_B = \oiint [(p\hat{n} - \boldsymbol{\tau}) + V\rho V \cdot \hat{n}] \, d\mathcal{S}_B \tag{12}$$

Outer-boundary force, momentum flow

$$F_O = \oiint -[(p - p_\infty)\hat{n} + (V - V_\infty)\rho V \cdot \hat{n}] \, d\mathcal{S}_O \tag{13}$$

In the F_B definition, the surface shear stress vector $\boldsymbol{\tau} = \bar{\bar{\tau}} \cdot \hat{n}$ has been introduced for convenience. In the F_O definition, p has been replaced with $p - p_\infty$, which is permissible because of the general relation

$$\oiint \hat{n} \, d\mathcal{S} = 0 \tag{14}$$

for any closed surface. Also, V has been replaced with $V - V_\infty$ which is permissible because of the mass relation (9).

The x axis is now chosen to lie along the flight path. Then, for steady unbanked flight at some climb angle γ, in a still atmosphere, we have

$$F_B = F_O = F_x\hat{x} + 0\hat{y} + F_z\hat{z} \tag{15}$$

$$-F_x = W \sin\gamma \tag{16}$$

$$F_z = W \cos\gamma \tag{17}$$

where F_x is the net streamwise aerodynamic force, F_z is the net normal aerodynamic force, and W is the weight. F_x will now be related to the outer-boundary integral in the F_O definition.

C. Streamwise Force Decomposition

With the Trefftz plane and side cylinder boundaries defined perpendicular and parallel to V_∞, the streamwise x component of the outer force (13) reduces to the following:

$$F_x = \iint -[(p - p_\infty) + \rho u(V_\infty + u)] \, d\mathcal{S}_O^{\text{TP}} + \iint -\rho u V_n \, d\mathcal{S}_O^{\text{SC}} \tag{18}$$

To put the first integral in Eq. (18) into a more convenient form, for later use with the kinetic energy analysis, we make the exact substitution

$$V_\infty u = \tfrac{1}{2}(V^2 - V_\infty^2) - \tfrac{1}{2}(u^2 + v^2 + w^2) \tag{19}$$

which gives a natural decomposition of the net streamwise force into three components:

$$F_x = F_u + F_v + F_n \tag{20}$$

$$F_u = \iint \left[(p_\infty - p) + \tfrac{1}{2}\rho(V_\infty^2 - V^2) - \tfrac{1}{2}\rho u^2 \right] d\mathcal{S}_O^{\text{TP}} \tag{21}$$

$$F_v = \iint \frac{1}{2}\rho(v^2 + w^2) \, d\mathcal{S}_O^{\text{TP}} \tag{22}$$

$$F_n = \iint -\rho u V_n \, d\mathcal{S}_O^{\text{SC}} \tag{23}$$

The F_u component is the net "profile drag–thrust" force associated with the axial perturbation velocity u. For low-speed flow and small $u \ll V_\infty$, it is effectively a total pressure defect

$$F_u \simeq \iint [p_{t_\infty} - p_t] \, d\mathcal{S}_O^{\text{TP}} - \mathcal{O}(\rho u^2) \tag{24}$$

whose integrand is negligible outside the viscous wakes and propulsion plumes. In contrast, the bulk of the F_v integrand in Eq. (22) comes from the trailing-vortex potential crossflow over the entire Trefftz plane, and hence is closely related to the induced drag D_i which will be discussed later. The remaining F_n term is zero for a sufficiently distant side cylinder in subsonic flow and equal to the far-field wave drag D_w in supersonic flow, which will also be discussed later.

In most force analyses of aircraft, F_u is typically separated into profile drag and thrust:

$$F_u = D_p - T \tag{25}$$

However, this decomposition is often ambiguous for aircraft whose propulsion system is closely integrated with the airframe and for aircraft which employ powered lift or boundary-layer control systems. It will be seen that, in the present power-based analysis, decomposition (25) is entirely unnecessary.

Most of the previous workers mentioned in the Introduction have further manipulated the F_u expression into equivalent forms in terms of entropy and total enthalpy. The F_v or D_i expression has also been manipulated into an equivalent form in terms of the crossflow stream function and the streamwise vorticity. Here, these alternative forms will not be used because they are not particularly useful in the subsequent mechanical energy analysis.

V. Mechanical Energy Analysis

A. Mechanical Energy Relation

Forming the dot product $\{\text{Eq.}\,(10)\} \cdot V$ gives the mechanical (kinetic) energy equation in divergence form:

$$\nabla \cdot \left(\rho V \tfrac{1}{2}V^2\right) = -\nabla p \cdot V + (\nabla \cdot \bar{\bar{\tau}}) \cdot V \tag{26}$$

Using the general vector identities

$$\nabla \cdot (pV) = \nabla p \cdot V + p\nabla \cdot V \tag{27}$$

$$\nabla \cdot (\bar{\bar{\tau}} \cdot V) = (\nabla \cdot \bar{\bar{\tau}}) \cdot V + (\bar{\bar{\tau}} \cdot \nabla) \cdot V \tag{28}$$

the right side of Eq. (26) is expanded as follows:

$$\nabla \cdot \left(\rho V \tfrac{1}{2}V^2\right) = -\nabla \cdot (pV) + p\nabla \cdot V + \nabla \cdot (\bar{\bar{\tau}} \cdot V) - (\bar{\bar{\tau}} \cdot \nabla) \cdot V \tag{29}$$

We now form the integral $\iiint \{\text{Eq.}\,(29)\} \, d\mathcal{V}$ over the entire CV, and apply relation (1) to give the following integral mechanical power balance equation

$$P_S + P_V + P_K = \dot{\mathcal{E}} + \Phi \tag{30}$$

where the five terms are defined in Eqs. (31–35). The substitutions $p \to p - p_\infty$ and $V^2 \to V^2 - V_\infty^2$ have been made as in the momentum equation analysis.

The three terms on the left side of Eq. (30) represent the total mechanical power supply, production, or inflow, ultimately from fuel, batteries, or other sources. The two terms on the right represent power consumption or outflow, via various physical processes. The balance holds instantaneously in steady flow or as a period average in unsteady-periodic flow. A major goal of the present paper is the determination of the total power required for flight, via the prediction and estimation of the right-hand side terms in Eq. (30) or its equivalents to be derived later.

Net propulsor shaft power

$$P_S = \oiint [-(p - p_\infty)\hat{n} + \boldsymbol{\tau}] \cdot V \, d\mathcal{S}_B \tag{31}$$

This is the integrated (force) · (velocity) on all moving body surfaces, and hence is the net total propulsor shaft power or wing-flapping power for all the components on the aircraft that are covered by the body control volume surface $\mathcal{S}_B$. If individual turbomachinery component blading is defined to be covered by $\mathcal{S}_B$, such as for the upper propulsor in Fig. 1, then P_S will include positive contributions from a compressor and negative contributions from a turbine. If the aircraft has powered lift or other boundary-layer control systems whose impeller blades are covered by $\mathcal{S}_B$, then P_S will also include the shaft power of the impellers.

Net pressure-volume "$P\, dV$" power

$$P_V = \iiint (p - p_\infty)\nabla \cdot \mathbf{V}\, d\mathcal{V} \qquad (32)$$

This is a volumetric (or $P\, dV$) mechanical power provided by the fluid expanding against atmospheric pressure. Its integrand will have strong net contributions at locations wherever heat is added at a pressure far from ambient, for example, if a turbomachinery combustor is chosen to be inside the CV or if external combustion is present, as in some hypersonic vehicles. In supersonic wave regions, the P_V integrand may be nonzero, but will cancel when integrated over all points whose streamlines reversibly return to the freestream state before exiting the CV. Obtaining this cancellation is the main motivation behind defining the CV such that the wave system exits through the side cylinder and ahead of the Trefftz plane.

Net propulsor mechanical energy flow rate into the CV

$$P_K = \oiint -\left[(p - p_\infty) + \tfrac{1}{2}\rho(V^2 - V_\infty^2) \right] \mathbf{V} \cdot \hat{n}\, d\mathcal{S}_B \qquad (33)$$

This is the net pressure-work rate and kinetic energy flow rate across $\mathcal{S}_B$ and into the CV. This accounts for power sources whose moving blading is not covered by $\mathcal{S}_B$ or whose combustors are outside the CV, such as the bottom propulsor in Fig. 1. Note that $\hat{n}$ points into the propulsor, so that the nozzle has $\mathbf{V} \cdot \hat{n} < 0$, and $P_K > 0$ for a propulsor with net thrust, as expected.

Mechanical energy flow rate out of the CV

$$\dot{\mathcal{E}} = \iint \left[(p - p_\infty) + \tfrac{1}{2}\rho(V^2 - V_\infty^2) \right](V_\infty + u)\, d\mathcal{S}_O^{\mathrm{TP}}$$
$$+ \iint \left[(p - p_\infty) + \tfrac{1}{2}\rho(V^2 - V_\infty^2) \right] V_n\, d\mathcal{S}_O^{\mathrm{SC}} \qquad (34)$$

This is the net pressure-work rate and kinetic energy flow rate out of the CV, through the Trefftz plane and side cylinder boundaries.

Viscous dissipation rate

$$\Phi = \iiint (\bar{\bar{\tau}} \cdot \nabla) \cdot \mathbf{V}\, d\mathcal{V} \qquad (35)$$

This measures the rate at which kinetic energy of the flow is converted into heat inside the CV. The dissipation mechanism is the viscous stresses $\bar{\bar{\tau}}$ working against fluid deformation, the latter related to the velocity gradients ∇V. In practice, most of the dissipation occurs in the thin boundary layers on the aircraft surface, including the propulsion elements, and also in shock waves. If powered lift or boundary-layer control systems are present, then the air in the suction or blowing plumbing can be considered as part of the flowfield, and the dissipation inside the plumbing would contribute to the overall Φ. Additional dissipation also occurs in the downstream wakes and jets, as shown in Fig. 2 and discussed later.

B. Energy-Outflow Rate Decomposition

The total energy rate $\dot{\mathcal{E}}$ definition Eq. (34) captures the outflow of all mechanical energy regardless of type or origin, making the power balance Eq. (30) somewhat difficult to apply and interpret. To clarify the situation, we now use the F_x definition Eq. (18), the weight relation (16), and the velocity relation (19), and exactly decompose $\dot{\mathcal{E}}$ into five separate components:
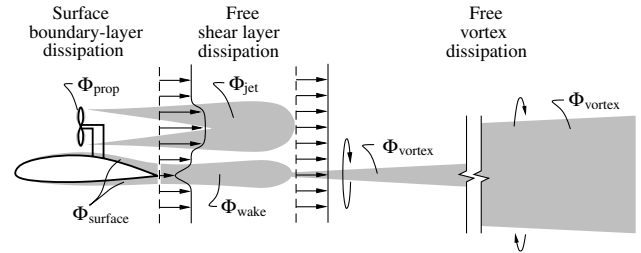
Fig. 2 Dissipation in various flow regions inside the CV. Not shown is additional dissipation which may occur inside any flow-control system ducting. Also not shown is dissipation in shock waves.

$$\dot{\mathcal{E}} = W\dot{h} + \dot{E}_a + \dot{E}_v + \dot{E}_p + \dot{E}_w \qquad (36)$$

each of which has a relatively clear physical origin. The result is the following alternative and equivalent form of the integral power balance equation:

$$P_S + P_V + P_K = W\dot{h} + \dot{E}_a + \dot{E}_v + \dot{E}_p + \dot{E}_w + \Phi \qquad (37)$$

where the five $\dot{\mathcal{E}}$ components are defined next.

Potential energy rate

$$W\dot{h} = -F_x V_\infty = W V_\infty \sin\gamma \qquad (38)$$

This is simply the power consumption needed to increase the aircraft's potential energy and becomes a power source during descent. The decomposition (37) therefore isolates this reversible $\dot{\mathcal{E}}$ component, leaving the remaining four components to capture all the irreversible outflow losses.

Wake streamwise kinetic energy deposition rate

$$\dot{E}_a = \iint \frac{1}{2}\rho u^2 (V_\infty + u)\, d\mathcal{S}_O^{\mathrm{TP}} \qquad (39)$$

This is the rate of streamwise kinetic energy being deposited in the flow out of the CV, through the Trefftz plane. Note that this is always positive, both in the case of a propulsive jet where the axial perturbation velocity u is positive and also for a wake where u is negative (assuming no reverse flow in the Trefftz plane, or $V_\infty + u > 0$).

Wake transverse kinetic energy deposition rate

$$\dot{E}_v = \iint \frac{1}{2}\rho(v^2 + w^2)(V_\infty + u)\, d\mathcal{S}_O^{\mathrm{TP}} \qquad (40)$$

This is the rate of transverse kinetic energy being deposited in the flow out of the CV. For $u \ll V_\infty, v, w$, this is in fact the same as V_∞ times the induced drag D_i for the case of a relatively nearby Trefftz plane where the vortex wake has not yet dissipated significantly.

Wake pressure-defect work rate

$$\dot{E}_p = \iint (p - p_\infty)u\, d\mathcal{S}_O^{\mathrm{TP}} \qquad (41)$$

This is the rate of pressure work done on the fluid crossing the Trefftz plane at some pressure p different from the ambient p_∞.

Wave pressure-work and kinetic energy outflow rate

$$\dot{E}_w = \iint \left[p - p_\infty + \tfrac{1}{2}\rho(u^2 + v^2 + w^2) \right] V_n\, d\mathcal{S}_O^{\mathrm{SC}} \qquad (42)$$

This is the pressure-work rate and kinetic energy deposition rate of the fluid crossing the side cylinder. Normally this will be significant only in supersonic flows, in which the $\dot{E}_w$ integrand on $\mathcal{S}_O^{\mathrm{SC}}$ is dominated by the oblique wave system, for which the integrated contribution to $\dot{E}_w$ is equal to the wave-drag power.

For subsonic 3-D flows, the $\dot{E}_w$ integrand for a lifting wing rapidly decays as $1/r^4$ and hence becomes negligible for a sufficiently distant side cylinder. For a relatively nearby side cylinder, the $\dot{E}_w$

integral is nonzero for a subsonic wing, but in this case it merely accounts for the transverse kinetic energy not fully captured in $\dot{E}_v$ because of the small Trefftz plane that accompanies a nearby side cylinder.

VI. Energy-Outflow Estimation and Characterization

The power balance relation (37), together with the $\dot{E}$ component definitions from earlier, is exact as written and does not require identification of rotational and irrotational regions over the Trefftz plane. However, it is useful to briefly identify such regions to compare relation (37) to previous force-based analyses.

A. Potential-Flow Regions in Low-Speed Flow

Outside of the viscous wakes and propulsion plumes, the pressure defect in low-speed flow is given by the Bernoulli relation:

$$p - p_\infty = -\tfrac{1}{2}\rho(V^2 - V_\infty^2) = -\rho V_\infty u - \tfrac{1}{2}\rho(u^2 + v^2 + w^2) \quad (43)$$

The sum of the three Trefftz plane $\dot{E}$ components then reduces exactly to the standard induced drag expression times V_∞:

$$\dot{E}_a + \dot{E}_v + \dot{E}_p = \iint \frac{1}{2}\rho(v^2 + w^2 - u^2)V_\infty \, d\mathcal{S}_O^{TP} \quad (44)$$

$$= D_i V_\infty \quad (45)$$

This sheds further light on the somewhat perplexing $-u^2$ term in the D_i integrand, which seems to run counter to kinetic energy arguments. The negative sign originates from the pressure-work term $\dot{E}_p$, which is negative and twice as large as the true axial kinetic energy loss term $\dot{E}_a$. The same pressure-work mechanism was recently identified by Spalart [10] via his entirely different force-based analysis.

B. Wave System

For any small-disturbance Mach wave, the following relations can be obtained from oblique-shock theory:

$$p - p_\infty = -\rho u V_\infty - \tfrac{1}{2}\rho u^2 M_\infty^2 \quad (46)$$

$$u^2 M_\infty^2 = u^2 + v^2 + w^2 \quad (47)$$

The $\dot{E}_w$ component then becomes

$$\dot{E}_w = \iint -\rho u V_n V_\infty \, d\mathcal{S}_O^{SC} \quad (48)$$

$$= D_w V_\infty \quad (49)$$

and, as expected, the energy loss rate from the outgoing wave system is simply the power needed to overcome the far-field wave drag.

C. Inviscid Flow Examples: Two-Dimensional Airfoil and Three-Dimensional Wing

For the simple case of an inviscid low-speed 2-D airfoil, the perturbation velocities at distances greater than the chord rapidly asymptote to those of a point vortex having the airfoil's circulation Γ. The energy rate integrals can then be readily evaluated for an infinite Trefftz plane at some location $x > \mathcal{O}(c)$:

$$\dot{E}_a = \frac{\rho V_\infty \Gamma^2}{8\pi} \frac{b}{x} \quad (50)$$

$$\dot{E}_v = \frac{\rho V_\infty \Gamma^2}{8\pi} \frac{b}{x} \quad (51)$$

$$\dot{E}_p = -\frac{\rho V_\infty \Gamma^2}{4\pi} \frac{b}{x} \quad (52)$$

$$\dot{E}_a + \dot{E}_v + \dot{E}_p = 0 \quad (53)$$

where b is the arbitrary span of the integration. Although the individual $\dot{E}$ components are quite large near the airfoil due to their $1/x$ behavior, they sum up exactly to zero for this inviscid 2-D case. This can also be seen from the original total $\dot{\mathcal{E}}$ definition (34), in which the integrand is zero for this constant total pressure case. This inviscid case also has $\Phi = 0$, and so the net required power as given by Eq. (37) is zero as well, as expected.

Figure 3 compares the variation of the three Trefftz plane $\dot{E}$ components Eqs. (50–52) for the 2-D airfoil, with the corresponding components for a lifting inviscid 3-D wing, the latter integrated numerically for a rigid wake with spanwise elliptical loading.

In the 3-D wing case, the total energy loss rate is also constant, but equal to $D_i V_\infty$ rather than zero. In 3-D, the individual $\dot{E}$ components also decay much faster than in the 2-D case, with each component very nearly reaching its final value within a fraction of the span b:

$$\dot{E}_a + \dot{E}_v + \dot{E}_p = D_i V_\infty \sim \rho V_\infty \Gamma^2 \quad (54)$$

for the 3-D wing.

In the subsequent discussions, these 2-D and 3-D potential-near-field transients in the individual $\dot{E}_a$, $\dot{E}_v$, $\dot{E}_p$ components will be excluded, because they cancel in the overall $\dot{E}$ sum.

D. Viscous Flow Power Balance Versus Trefftz Plane Location

It is important to note that Eq. (37) holds for any position of the side cylinder and Trefftz plane boundaries, provided Φ is defined as only the dissipation inside the CV. Figure 4 shows how the individual terms in Eq. (37) vary as the Trefftz plane is progressively moved downstream.

The $\dot{E}_a$ term defined by Eq. (39), initially equal to some fraction of the net axial-force power $F_u V_\infty$, decays relatively quickly as the axial velocity perturbation u decays by mixing and diffusion, with the lost energy appearing as the $\Phi_{wake} + \Phi_{jet}$ part of the overall dissipation Φ. After a much greater distance downstream, the transverse velocities v, w of the trailing vortices also eventually diffuse, and the transverse kinetic energy integral $\dot{E}_v$, initially equal to $D_i V_\infty$, decays accordingly. Again, the dissipation Φ is correspondingly increased by the Φ_{vortex} part, so that the total power remains unchanged.

VII. Dissipation Estimation and Characterization

A. Dissipation in Trailing Vortices

As indicated by Figs. 2 and 4, all power sources P_P, P_V, P_K in excess of the potential energy rate $W\dot{h}$ are eventually balanced by the
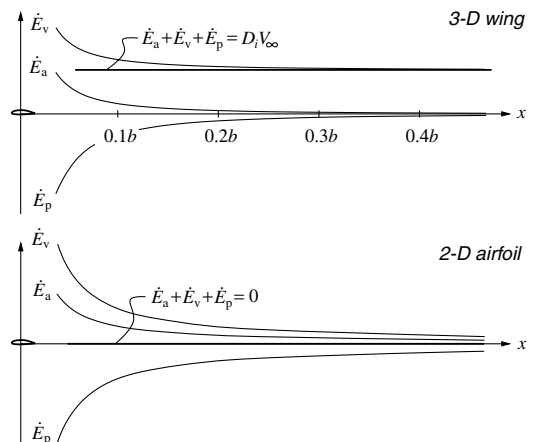

Fig. 3 Energy loss rate components versus position of Trefftz plane for inviscid 2-D airfoil and inviscid 3-D wing. For 2-D airfoil, the total loss rate is zero. For 3-D wing, the total loss rate is constant and equal to $D_i V_\infty$. The individual $\dot{E}_a, \dot{E}_v, \dot{E}_p$ terms asymptote very rapidly in the 3-D case.
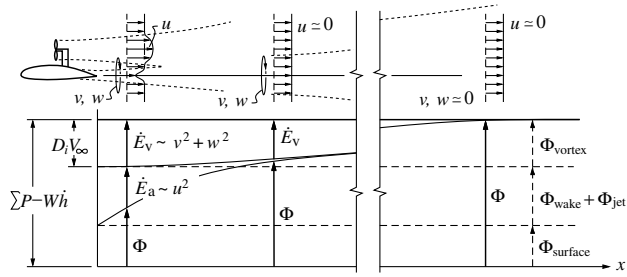
Fig. 4 Variation in power balance terms in Eq. (37) versus position of Trefftz plane. Transverse velocities of trailing vortices diffuse much later than the axial velocities of propulsors and wakes. Total dissipated power sum is unchanged. The potential-near-field contributions to $\dot{E}_a$, $\dot{E}_v$ are excluded, $\dot{E}_p$ is not shown, and $\dot{E}_w$ is assumed to be zero.

dissipation Φ if the Trefftz plane is extended sufficiently far downstream. In practice, it is advantageous to place the Trefftz plane close enough so that the $\dot{E}_v \simeq D_i V_\infty$ contribution from the dissipation of trailing vortices can be kept separate in the power balance in Eq. (37). The reason is that D_i can be reliably estimated by other relations, such as the classical result for a planar elliptically loaded wing without thrust vectoring, for which $F_z = L$:

$$D_i = \frac{L^2}{\frac{1}{2}\rho V_\infty^2 \pi b^2} \qquad (55)$$

Hence, with such alternative $\dot{E}_v$ calculation methods being available, $\dot{E}_v$ or Φ_{vortex} do not need to be calculated directly from their definitions.

B. Dissipation in Propulsor Jets

The jet dissipation Φ_{jet} of the isolated propulsor indicated in Fig. 2 represents the Froude propulsive (in)efficiency, and hence can be calculated from the disk loading and actuator-disk theory, or from propeller theory, or simply from known propulsor performance:

$$\Phi_{\text{jet}} = P_S(1 - \eta_{\text{Froude}}) \qquad (56)$$

As with Φ_{vortex}, such alternative models eliminate the need to calculate Φ_{jet} directly. If Eq. (56) is used, then it is simplest to lump it into the left side of Eq. (37) by replacing P_S with $\eta_{\text{Froude}} P_S$.

C. Dissipation on Propulsor Blading

The Φ_{prop} in Fig. 2 represents the dissipation in the propulsor's blading boundary layers and is otherwise known as profile losses. This can be computed directly via integration over the blade surface using the dissipation coefficient (discussed later) or by radial blade-element integration using the blade profile-drag coefficients, or simply by a known overall profile efficiency if that's available:

$$\Phi_{\text{prop}} = P_S(1 - \eta_{\text{profile}}) \qquad (57)$$

D. Dissipation and Power Loss in Shock Waves

The presence of shock waves will make the various terms in the power balance relation (37) have additional contributions. Figure 5 shows the various shocks which might be present on a transonic or supersonic aircraft. The losses of the nearby strong shocks are best added via the dissipation term Φ, whereas the losses of the distant waves are best added via the $\dot{E}_w$ term.

1. Nearby Strong-Shock Losses

The dissipation of a shock is given by

$$\Phi_{\text{shock}} \simeq \iint \Delta p_t V \cdot \hat{n}_{\text{shock}} \, d\mathcal{S}_{\text{shock}} \qquad (58)$$
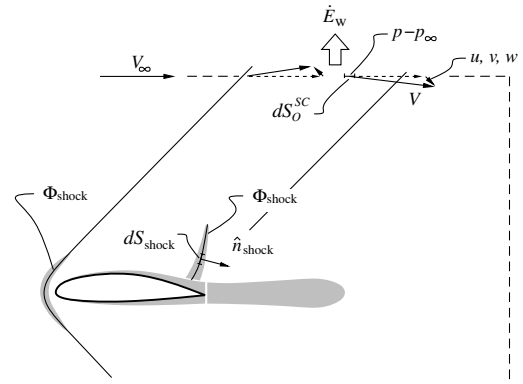
Fig. 5 Dissipation in strong shocks near aircraft and wave pressure-work and kinetic energy outflow through the side cylinder.

where the integration is over the shock surface with unit normal $\hat{n}_{\text{shock}}$. The total pressure drop Δp_t depends on the normal Mach number $M_\perp$ via standard normal-shock relations.

2. Outer Wave System Losses

The integrand in Eq. (58) scales as $\Delta p_t \sim (M_\perp - 1)^3$, which becomes very small as the waves propagate away from the aircraft, where $M_\perp \to 1$. The dissipation therefore requires a great distance to run to completion, and hence is better represented by the $\dot{E}_w$ term in the power balance Eq. (37), as discussed previously, and estimated by Eq. (48). This $\dot{E}_w$ can be determined by various wave-drag D_w estimation methods, such as those of Jones [14] for linearized supersonic flow.

E. Dissipation in Shear Layers and Wakes

Because the components of Φ and $\dot{E}$ associated with induced drag, propulsion losses, and shock waves can be expressed or estimated as discussed earlier, we then only need to consider the remaining dissipation components Φ_{surface} and Φ_{wake} due to the surface boundary layers and trailing wakes. For the remainder of the paper we define x, y, z to be the traditional locally Cartesian shear layer coordinates, where x, z lie on the surface and y is normal to the surface and across the shear layer, as shown in Fig. 6. Also, u, w will denote the total x,z velocity components.

The dissipation integrand in Eq. (35), which in full contains nine terms, reduces to only two dominant terms in a 3-D shear layer

$$\Phi \simeq \iiint \left(\tau_{xy} \frac{\partial u}{\partial y} + \tau_{zy} \frac{\partial w}{\partial y} \right) dx \, dy \, dz \qquad (59)$$

or just one term in a 2-D shear layer

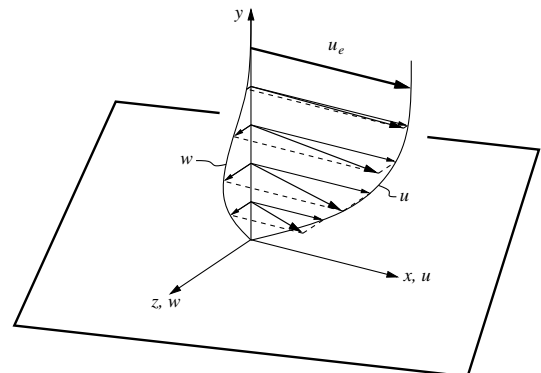$$\Phi \simeq \iiint \tau_{xy} \frac{\partial u}{\partial y} \, dx \, dy \, dz \qquad (60)$$

Fig. 6 Boundary-layer profile on surface, with locally Cartesian x, y, z axes. The x axis is defined to lie along edge velocity u_e.

A 2-D shear layer is defined as one with a planar velocity profile, or $w = 0$. For brevity in the subsequent discussion, the 2-D form will be assumed. The w term can always be added if needed to give the 3-D form.

The shear stress consists of the laminar plus turbulent Reynolds stress:

$$\tau_{xy} = \mu \frac{\partial u}{\partial y} - \rho \overline{u'v'} \tag{61}$$

$$\Phi = \iiint \left[\mu \left(\frac{\partial u}{\partial y} \right)^2 - \rho \overline{u'v'} \frac{\partial u}{\partial y} \right] dx \, dy \, dz \tag{62}$$

Since $-\rho \overline{u'v'}$ in conventional shear layers has the same sign as $\partial u / \partial y$, the dissipation integrand is strictly positive, as expected.

1. Dissipation Coefficient

For a shear layer, it is convenient to express Φ_{surface}, Φ_{prop}, or Φ_{wake} in terms of a dissipation coefficient $C_{\mathcal{D}}(x, z)$ defined for each point on the shear layer:

$$\Phi = \iint \rho_e u_e^3 C_{\mathcal{D}} \, dx \, dz \tag{63}$$

This is directly analogous to defining friction drag in terms of a skin friction coefficient,

$$D_f = \iint \frac{1}{2} \rho_e u_e^2 C_f \, dx \, dz \tag{64}$$

except that $C_{\mathcal{D}}$ is nonzero on a wake.

Using $C_{\mathcal{D}}$ rather than C_f has a number of advantages:

1) $C_{\mathcal{D}}$ and Φ capture all drag-producing loss mechanisms. In contrast, C_f and D_f still leave out the pressure-drag contribution.

2) $C_{\mathcal{D}}$ and Φ are scalars, and so the orientation of the $dx \, dz$ surface element in the Eq. (63) integral is immaterial. In contrast, Eq. (64) represents a force vector integral and, as written, is strictly correct only for flat-plate surfaces aligned with the freestream flow.

3) $C_{\mathcal{D}}$ is strictly positive, and so there are no force-cancellation problems which often occur with near-field force integration.

2. Boundary Layer and Wake Thicknesses

Various shear layer properties can be given in terms of the following integral thicknesses and defects:

Mass defect

$$\rho_e u_e \delta^* = \int_0^{y_e} (\rho_e u_e - \rho u) \, dy \tag{65}$$

Momentum defect

$$\rho_e u_e^2 \theta = \int_0^{y_e} (u_e - u) \rho u \, dy \tag{66}$$

Kinetic energy defect

$$\rho_e u_e^3 \theta^* = \int_0^{y_e} (u_e^2 - u^2) \rho u \, dy \tag{67}$$

Density defect

$$\rho_e u_e \delta^{**} = \int_0^{y_e} (\rho_e - \rho) u \, dy \tag{68}$$

Wake kinetic energy excess

$$\rho_e u_e^3 \delta_K = \int_0^{y_e} (u_e - u)^2 \rho u \, dy \tag{69}$$

We also note the following useful identity:

$$\delta_K = 2\theta - \theta^* \tag{70}$$

Both θ and θ^* obey the von Kármán integral momentum equation and the corresponding integral kinetic energy equation:

$$\frac{d(\rho_e u_e^2 \theta)}{dx} = \rho_e u_e^2 \tfrac{1}{2} C_f - \rho_e u_e \delta^* \frac{du_e}{dx} \tag{71}$$

$$\frac{d(\tfrac{1}{2} \rho_e u_e^3 \theta^*)}{dx} = \rho_e u_e^3 C_{\mathcal{D}} - \rho_e u_e^2 \delta^{**} \frac{du_e}{dx} \tag{72}$$

The density-flux thickness δ^{**} term in Eq. (72) represents ramjet thrust effects and is significant only in very high-speed or non-adiabatic boundary layers with strong pressure gradients. If this term is negligible, as with most external aerodynamic flows, from Eq. (72), we see that, in 2-D flow of unit span, $\rho_e u_e^3 \theta^*$ at any location measures all the upstream dissipation:

$$\tfrac{1}{2} \rho_e u_e^3 \theta^*(x) = \int_0^x \rho_e u_e^3 C_{\mathcal{D}} \, dx = \Phi(x) \tag{73}$$

The various thicknesses can also be used to specify the various integral quantities at the Trefftz plane,

$$F_u = \int_{z_{\min}}^{z_{\max}} \rho_e u_e^2 \theta \, dz \tag{74}$$

$$\dot{E}_a = \int_{z_{\min}}^{z_{\max}} \frac{1}{2} \rho_e u_e^3 \delta_K \, dz \tag{75}$$

where the z integration would be over the spanwise extent of the wake.

VIII. Power Balance in Simple Cases

We now examine the various terms in Eq. (37) for simple cases to relate these to more familiar drag-related quantities.

A. Two-Dimensional Airfoil

In this case, we assume that the airfoil is propelled at a steady speed by an isolated ideal propulsor that does not interact with the airfoil's immediate flowfield. The propulsor provides only the thrust T necessary to oppose the drag D (equal to profile drag in this 2-D case). If the ideal propulsor works against the same freestream velocity as the airfoil, it will expend power $P_{\text{isolated}} = TV_\infty$ to sustain the thrust. Because there is no induced drag in this 2-D flow, Eq. (37) reads

$$TV_\infty = P_{\text{isolated}} = \dot{E}_a + \Phi \tag{76}$$

We now choose the Trefftz plane to be sufficiently far downstream so that $\dot{E}_a$ effectively disappears, and we also replace T with D:

$$DV_\infty = P_{\text{isolated}} = \Phi_{\text{total}} \tag{77}$$

Hence, the total dissipation in the flowfield in this case is simply equal to the drag power DV_∞, which is also the power expended by the isolated propulsor.

B. Two-Dimensional Airfoil with Wake Ingestion

This case is the same as the preceding case, except that the ideal propulsor is now placed at the airfoil trailing edge and generates a "perfect" filled-in wake with $u = 0$ everywhere. This is consistent with Eq. (21), which indicates a zero net axial force $F_u = 0$ if $u = 0$. We note that, in this case, $\dot{E}_a = 0$ everywhere, so that the same Φ is obtained for any Trefftz plane location and, in particular, all contributions to Φ occur only on the airfoil surface. Equation (37) then gives the wake-ingesting propulsor power as

$$P_{\text{ingest}} = \Phi_{\text{surface}} \tag{78}$$

where Φ_{surface} denotes the dissipation occurring in the airfoil surface boundary layers. Note that there is no need to consider or even define

thrust or drag, which are not even well defined for this case. Nevertheless, the propulsive power remains well defined.

It is of particular interest to compare the noningesting power from Eq. (77) with the ingesting power from Eq. (78):

$$P_{isolated} - P_{ingest} = \Phi_{total} - \Phi_{surface} \qquad (79)$$

Referring to Fig. 4 or Fig. 7, it is evident that this power difference is simply Φ_{wake}, which is the additional Φ contribution of the noningested airfoil wake, which is also equal to the kinetic energy flux off the trailing edge (TE):

$$P_{isolated} - P_{ingest} = \dot{E}_{a_{TE}} \qquad (80)$$

Hence, the benefit of wake ingestion is that it eliminates the downstream dissipation in the wake, equal to $\dot{E}_a$ at that location, which would otherwise occur. For maximum benefit, the ingestion must be done at the point of maximum $\dot{E}_a$, which is at or near the trailing edge for most airfoils.

C. Flat Plate with Boundary Layer and Wake

We now compute the drag on a laminar flat plate of unit span and chord c in three ways, summarized next. In this case, the edge velocity $u_e = V_\infty$ is constant, and the surface C_f and $C_\mathcal{D}$ coefficients are known in terms of the x-based Reynolds number:

$$\tfrac{1}{2}C_f = 0.332(u_e x/\nu)^{-1/2} \qquad (81)$$

$$C_\mathcal{D} = 0.261(u_e x/\nu)^{-1/2} \qquad (82)$$

1) Skin friction integration

$$D = \int_0^c \rho_e u_e^2 \tfrac{1}{2} C_f \, dx \qquad (83)$$

$$= 0.664 \rho_\infty V_\infty^2 c Re_c^{-1/2} \qquad (84)$$

2) Dissipation integration on surface and wake (Trefftz plane far downstream)

$$DV_\infty = \int_0^c \rho_e u_e^3 C_\mathcal{D} \, dx + \int_c^\infty \rho_e u_e^3 C_\mathcal{D} \, dx \qquad (85)$$

$$= 0.522 \rho_\infty V_\infty^3 c Re_c^{-1/2} + \Phi_{wake} \qquad (86)$$

3) Dissipation integration on surface, plus wake kinetic energy flux (Trefftz plane at trailing edge)

$$DV_\infty = \int_0^c \rho_e u_e^3 C_\mathcal{D} \, dx + (\tfrac{1}{2}\rho_e u_e^3 \delta_K)_{x=c} \qquad (87)$$

$$= 0.522 \rho_\infty V_\infty^3 c Re_c^{-1/2} + \dot{E}_{a_{TE}} \qquad (88)$$

Relations (86) and (88) are clearly the same, since $\Phi_{wake} = (\dot{E}_a)_{TE}$ as diagrammed by Fig. 7. They must also be consistent with Eq. (84).
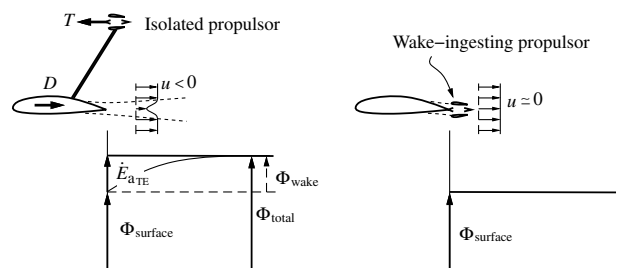
Fig. 7 Comparison of dissipation in isolated and wake-ingesting propulsors for 2-D airfoil.

Setting the two drag results Eqs. (84) and (88) equal, we get a numerical value for $(\dot{E}_a)_{TE}$, or equivalently for Φ_{wake}

$$0.522 \rho_\infty V_\infty^3 c Re_c^{-1/2} + \dot{E}_a = 0.664 \rho_\infty V_\infty^3 c Re_c^{-1/2} \qquad (89)$$

$$\dot{E}_a = 0.142 \rho_\infty V_\infty^3 c Re_c^{-1/2} \qquad (90)$$

For the general airfoil case, it may be more convenient to compute or estimate $\dot{E}_a$ using the identity Eq. (70),

$$\dot{E}_a = \tfrac{1}{2}\rho_e u_e^3 \delta_K = \rho_e u_e^3 \theta - \tfrac{1}{2}\rho_e u_e^3 \theta^* = \tfrac{1}{2}\rho_e u_e^3 \theta^* \left(\frac{2}{H^*} - 1\right) \qquad (91)$$

and an assumed value of H^*, which takes on the following typical narrow range of values:

$$H^* \simeq \begin{cases} 1.50, & \text{laminar or turbulent separated flow} \\ 1.60, & \text{laminar attached flow} \\ 1.75, & \text{turbulent attached flow} \end{cases} \qquad (92)$$

The trailing edge $\dot{E}_a$ value Eq. (90) indicates that for a laminar flat plate, a quite substantial fraction $0.142/0.664 = 21\%$ of the energy losses occur in the wake. This can be seen in Fig. 8, which shows the kinetic energy defect $\rho_e u_e^3 \theta^*$ distribution along the plate, which measures the accumulated dissipation via Eq. (73). The implication is that an ideal wake-ingesting propulsor for a laminar flat plate could have up to 21% less power consumption than a noningesting propulsor.

D. Two-Dimensional Airfoil

In the case of an airfoil, the skin friction integration Eq. (84) must now be extended to include the pressure drag and must now be carried into the wake:

$$D = \int_0^c \rho_e u_e^2 \tfrac{1}{2} C_f \, dx + \int_0^\infty -\rho_e u_e \delta^* \frac{du_e}{dx} \, dx \qquad (93)$$

In contrast, the dissipation integrals (86) or (88) still have exactly the same form:

$$DV_\infty = \int_0^c \rho_e u_e^3 C_\mathcal{D} \, dx + \int_c^\infty \rho_e u_e^3 C_\mathcal{D} \, dx \qquad (94)$$

Figure 9 shows the $\rho_e u_e^3 \theta^*$ distributions for the top and bottom surface and wake of a transonic airfoil at high Reynolds number. In this case, the wake dissipation is about 13% of the total, which is still large enough to make wake recovery an attractive possibility. The airfoil also has laminar flow up to $x = 0.7$ on the bottom surface, which is responsible for the very low $\rho_e u_e^3 \theta^*$ growth up to that point.
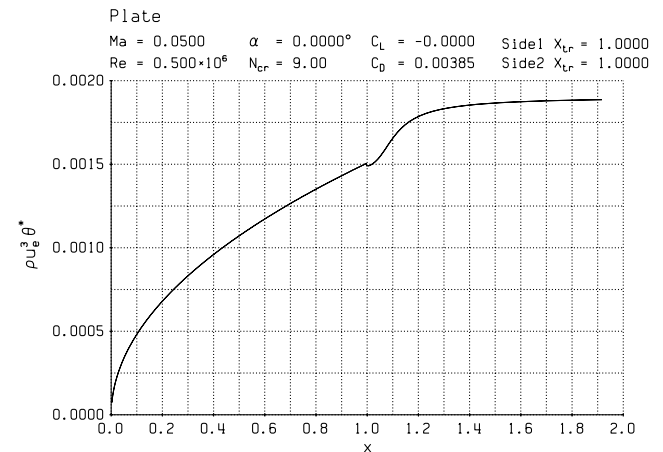

Fig. 8 Kinetic energy defect $\rho_e u_e^3 \theta^*$ distribution on a laminar flat plate. This shows the accumulating dissipation on the surface and in the wake that starts at $x = 1$.
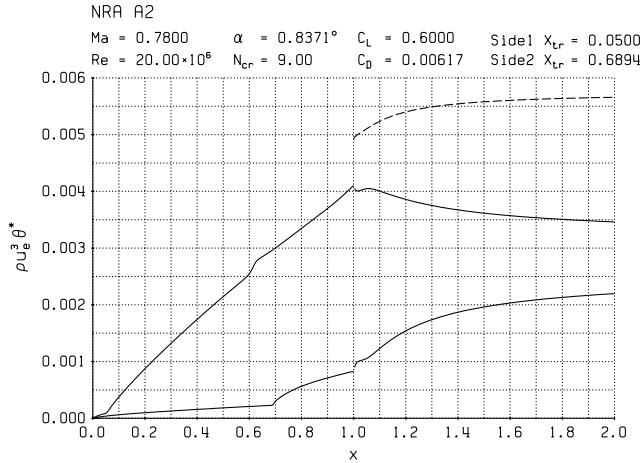
Fig. 9 Transonic airfoil $\rho_e u_e^3 \theta^*$ distributions on top and bottom surfaces and wake halves, and for wake total (dashed line).

Fig. 11 $C_\mathcal{D}$ and $C_f/2$ versus H for turbulent boundary layers for $Re_\theta = 200, 1000, 5000$.

E. Dissipation and Skin Friction Coefficients in Shear Layers

1. Dependence on Shape Parameter, Reynolds Number

The boundary-layer shape parameter $H = \delta^*/\theta$ directly indicates the state of the boundary layer and, in particular, how close the boundary layer is to separation. Figure 10 shows $C_\mathcal{D}$ and $C_f/2$ dependence on H for laminar boundary layers. These scale as $1/Re_\theta$, so that the $Re_\theta C_\mathcal{D}$ and $Re_\theta C_f/2$ values are independent of Re_θ. Note that the laminar $C_\mathcal{D}$ is very nearly independent of H, meaning that laminar boundary-layer losses are almost entirely dependent on the Reynolds number and nearly independent of pressure gradient.

Figure 11 shows the $C_\mathcal{D}$ and $C_f/2$ dependence on H for turbulent boundary layers. The $C_\mathcal{D}$ now has a clear minimum, close to the H value corresponding to a constant-pressure flow, and increases for both accelerating and decelerating flow. The rapid increase with H essentially represents pressure drag, which in the profile-drag expression Eq. (93) is captured by the second term. It should also be noted that the dependence of $C_\mathcal{D}$ on Re_θ for turbulent flow is much weaker than the $C_\mathcal{D} \sim 1/Re_\theta$ dependence for laminar flow.

The approximate spreading half-angle of 7 deg observed for a free shear layer [15] implies a dissipation coefficient of approximately

$$C_\mathcal{D} \simeq 0.02 \qquad (95)$$

This corresponds to an asymptotic value of $C_\mathcal{D}$ for $H \gg 1$ in Fig. 11.

2. Dependence on Flow Velocity

The dissipation expression Eq. (63) shows that, for any given $C_\mathcal{D}$ value, the physical boundary-layer losses scale as u_e^3. This implies that "overspeeds," or regions of high local u_e are very costly. Conversely, in regions of low velocity, such as in slat coves that have a fully separated recirculating flow, the losses are quite modest because of the small u_e^3 factor.
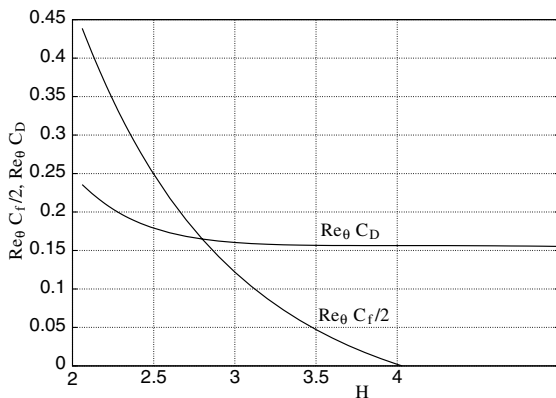
F. Dissipation-Based Drag Buildup

The u_e^3 factor in Eq. (63) has significant implications for excrescence and interference drag. Traditional excrescence drag estimates, as discussed by Hoerner [16] for example, scale the individual drag contributions with u_e^2 in accordance with a local dynamic-pressure argument. Any discrepancy is typically attributed to some uncertain additional interference drag. However, Eq. (63) clearly shows that a u_e^3 scaling is more appropriate. Furthermore, if no additional dissipation-causing flow structures (e.g., flow separation) are created, there should be no additional uncertain interference drag.

To illustrate the difference between force-based and dissipation-based drag buildup, consider a configuration consisting of a large and a small body, shown in Fig. 12. Their relative sizes are such that, when the bodies are far apart, the drags are 100 and 1 for a total drag of $D = 101$.

When the small body is placed near the large body where the local velocity is $V_2 = 2$, as shown in Fig. 13, the force-based drag buildup gives

$$D = \sum D_k = 100 + 4 = 104 \qquad (96)$$

whereas the dissipation-based buildup gives

$$D = \frac{1}{V_\infty} \sum \Phi_k = 100 + 8 = 108 \qquad (97)$$

which is a rather different result.

Viscous CFD calculations indicate that the dissipation-based buildup Eq. (97) is far more accurate than the force-based buildup Eq. (96). The reason is that Eq. (96) neglects the additional pressure drag on the large body, due to the potential source flow created by the viscous displacement on the small body. Traditionally, this might be
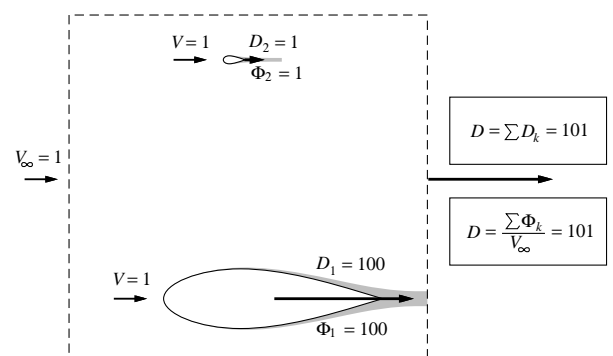
Fig. 10 $Re_\theta C_\mathcal{D}$ and $Re_\theta C_f/2$ versus H for laminar boundary layers.

Fig. 12 Drag buildup for two isolated bodies by force summation (top box) and dissipation summation (bottom box).
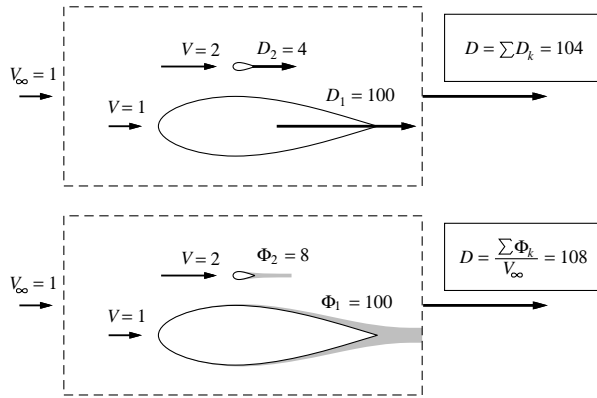
Fig. 13 Drag buildup for two closely interacting bodies by force summation (top) and dissipation summation (bottom). The small body is in the large body's near field and sees a doubled local velocity.

labeled interference drag of some possibly uncertain origin, but the mechanism and effect is captured quite well by the dissipation-based drag buildup Eq. (97).

G. Evaluation of Alternative Propulsion Systems

The efficiency benefit of wake ingestion is almost universally exploited in marine propulsion and has also been considered for aeronautical applications. The previous analyses, such as that of Smith [17], have typically computed the propulsor power reduction with the assumption that the ingested airframe boundary layer is given. However, computing or estimating the benefit of integrated/ingesting propulsion systems is far more complex, because the airframe flow is itself modified. An attractive feature of the present energy-based analysis is that comparison of such alternative propulsion systems is considerably simplified and the competing effects are clearly identified.

Figure 14 shows a traditional isolated propulsor and an alternative integrated propulsor driving a wing. The situation is a more complex version of the one in Figure 7 for two reasons: 1) the integrated propulsor now changes the airframe losses, and 2) there is now an excess thrust for both cases, typically needed to balance the induced drag and profile drag from other parts of the aircraft. The upper right drawing in Fig. 14 shows the pros, or the loss mechanisms that were eliminated or reduced in switching to the integrated system. These gains consist of removal of the two shear layers and their dissipation, and reduction of the excess wake kinetic energy by filling in of the large upper-surface boundary-layer momentum defect. The lower right drawing shows the cons, or the loss mechanisms that were added in the switch. Quantitative evaluation or estimation of all the pro and con changes shown in Fig. 14 would then give the net resulting change in the flight power:

$$\Delta P = \sum \Delta \dot{E} + \sum \Delta \Phi \qquad (98)$$

The sums on the right-hand side can, in principle, be carried out to any level of detail deemed appropriate. In addition to the first-level changes shown in Fig. 14, one could also account for changes in dissipation Φ_{prof} on the fan blading (e.g., fan profile efficiency), change in the total weight or span loading and resulting change in induced power $\dot{E}_v$, changes in shock losses Φ_{shock} if any, modification to the upper-cowl boundary-layer dissipation, etc.

IX. Conclusions

A control volume analysis of the flow about an aircraft has been performed, focusing on mechanical energy. The result is a concise relation between all the power sources and sinks in a flowfield, which has a number of useful applications:

1) The quantities which directly influence flight power requirements are clearly identified.

2) It is fully consistent with previous analyses based on momentum.

3) There is no need to define the rather ambiguous thrust or drag in configurations with tightly integrated propulsion systems.

4) The wake energy loss is clearly decomposed into independent contributions due to axial and transverse wake velocities without the need to separately identify rotational and irrotational regions of the Trefftz plane. This eliminates the ambiguity between thrust, profile drag, and induced drag in configurations where the viscous wakes and the vortex wakes are not distinct.

5) For traditional drag buildup analyses, using the power approach appears to be more reliable in that it accounts for interference effects that are not captured by the force approach.

Acknowledgment

References

[1] Betz, A., "Ein verfahren zur direkten ermittlung des profilwiderstandes," *Zeitschrift für Flugtechnik und Motorluftschiffahrt*, Vol. 16, Feb. 1925, pp. 42–44.

[2] Jones, B., "Measurement of Profile Drag by the Pitot-Traverse Method," Aeronautical Research Council R&M Rept. 1688, 1936.

[3] Oswatisch, K., "Der Verdichtungsstoss bei der Stationären Umströmung Flacher Profile," *ZAMM*, Vol. 29, 51949, pp. 129–141.
doi:10.1002/zamm.19490290501

[4] Maskell, E. C., "Progress Towards a Method of Measurement of the Components of the Drag of a Wing of Finite Span," Royal Aircraft Establishment TR 72232, Jan. 1973.

[5] Kroo, I., "Drag Due to Lift: Concepts for Prediction and Reduction," *Annual Review of Fluid Mechanics*, Vol. 33, Jan. 2001, pp. 587–617.
doi:10.1146/annurev.fluid.33.1.587

[6] VanDam, C., "Recent Experience with Different Methods of Drag Prediction," *Progress in Aerospace Sciences*, Vol. 35, No. 8, 1999, pp. 751–798.
doi:10.1016/S0376-0421(99)00009-3

[7] Giles, M. B., and Cummings, R. M., "Wake Integration for Three-Dimensional Flowfield Computations: Theoretical Development," *Journal of Aircraft*, Vol. 36, No. 2, 1999, pp. 357–365.
doi:10.2514/2.2465

[8] Kusunose, K., *A Wake Integration Method for Airplane Drag Prediction*, Tohoku Univ. Press, Sendai, Japan, 2005.

[9] Méheut, M., and Bailly, D., "Drag-Breakdown Methods from Wake Measurements," *AIAA Journal*, Vol. 46, No. 4, 2008, pp. 847–862.
doi:10.2514/1.29051

[10] Spalart, P. R., "On the Far Wake and Induced Drag of Aircraft," *Journal of Fluid Mechanics*, Vol. 603, May 2008, pp. 413–430.

[11] Denton, J. D., and Cumpsty, N. A., "Loss Mechanisms in Turbomachinery," Inst. of Mechanical Engineers Paper C260/87, 1987.

[12] Denton, J. D., "The 1993 IGTI Scholar Lecture: Loss Mechanisms in Turbomachinery," *Journal of Turbomachinery*, Vol. 115, No. 4, Oct. 1993, p. 621.
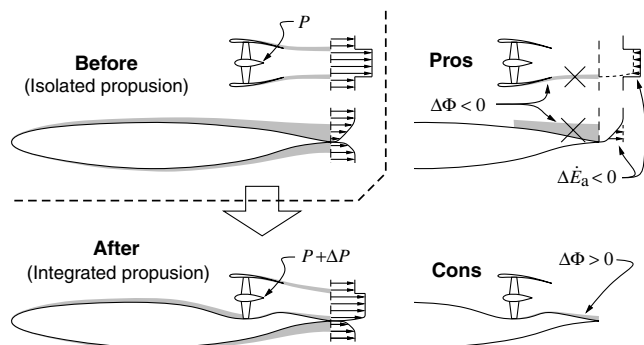

Fig. 14 Changes resulting from switch from isolated to distributed propulsion while keeping the same net streamwise momentum defect and force. Power change ΔP is the net result of negative (pro) and positive (con) $\Delta \Phi$ and $\Delta \dot{E}$ changes.

doi:10.1115/1.2929299

[13] Greitzer, E. M., Tan, C. S., and Graf, M. B., *Internal Flow: Concepts and Applications*, Cambridge Univ. Press, Cambridge, England, U.K., 2004.

[14] Jones, R. T., *Wing Theory*, Princeton Univ. Press, Princeton, NJ, 1990.

[15] White, F. M., *Viscous Fluid Flow*, McGraw–Hill, New York, 1974.

[16] Hoerner, S. F., *Fluid-Dynamic Drag*, Hoerner Fluid Dynamics, Vancouver, WA, 1965.

[17] Smith, L. H., Jr., "Wake Ingestion Propulsion Benefit," *Journal of Propulsion and Power*, Vol. 9, No. 1, Jan.–Feb. 1993, pp. 74–82. doi:10.2514/3.11487

E. Oran
Associate Editor